High-throughput lensfree 3D tracking of human sperms reveals rare statistics of helical trajectories

Ting-Wei Su[a,b], Liang Xue[a,b,c], and Aydogan Ozcan[a,b,d,e,1]

[a]Electrical Engineering Department, University of California, Los Angeles, CA 90095; [b]Bioengineering Department, University of California, Los Angeles, CA 90095; [c]Department of Information Physics and Engineering, Nanjing University of Science and Technology, Nanjing, Jiangsu 210094, China; [d]California NanoSystems Institute, University of California, Los Angeles, CA 90095; and [e]Department of Surgery, David Geffen School of Medicine, University of California, Los Angeles, CA 90095

Edited by Wallace F. Marshall, UCSF, San Francisco, CA, and accepted by the Editorial Board August 16, 2012 (received for review July 21, 2012)

Dynamic tracking of human sperms across a large volume is a challenging task. To provide a high-throughput solution to this important need, here we describe a lensfree on-chip imaging technique that can track the three-dimensional (3D) trajectories of >1,500 individual human sperms within an observation volume of approximately 8–17 mm^3. This computational imaging platform relies on holographic lensfree shadows of sperms that are simultaneously acquired at two different wavelengths, emanating from two partially-coherent sources that are placed at 45° with respect to each other. This multiangle and multicolor illumination scheme permits us to dynamically track the 3D motion of human sperms across a field-of-view of >17 mm^2 and depth-of-field of approximately 0.5–1 mm with submicron positioning accuracy. The large statistics provided by this lensfree imaging platform revealed that only approximately 4–5% of the motile human sperms swim along well-defined helices and that this percentage can be significantly suppressed under seminal plasma. Furthermore, among these observed helical human sperms, a significant majority (approximately 90%) preferred right-handed helices over left-handed ones, with a helix radius of approximately 0.5–3 μm, a helical rotation speed of approximately 3–20 rotations/s and a linear speed of approximately 20–100 μm/s. This high-throughput 3D imaging platform could in general be quite valuable for observing the statistical swimming patterns of various other microorganisms, leading to new insights in their 3D motion and the underlying biophysics.

human sperm imaging | sperm tracking | digital holography | micro-swimmer

Observing three-dimensional (3D) trajectories of sperms is in general a challenging task. This is partially due to limited imaging volume of optical microscopes that are based on conventional lenses. For human sperms this becomes even more challenging since the sperm head is small (approximately 3–4 μm) demanding a relatively high-magnification objective lens, and moves rather fast (20–100 μm/s) which makes it difficult to track their 3D swimming patterns as they quickly move out of the observation volume of an objective lens. Partly due to this low throughput and the limited spatial and temporal sampling windows that conventional microscopes provide, natural 3D swimming patterns of human sperms and their statistics could not be reported so far. Earlier results (1–19) that were obtained using lens-based conventional microscopes either measured the 2D trajectories of the human sperms along a focal plane, or reported on sperms of other species such as sea urchin, which were significantly easier to resolve under a microscope since their 3D rotation diameter is larger (>13 μm) together with a lower rotation frequency compared to human sperms.

Here we report a new technique that is based on lensfree holographic imaging on a chip to dynamically track the 3D trajectories of human sperms across a large volume of approximately 8–17 mm^3 (Fig. 1) with submicron positioning accuracy. This platform can track >1,500 individual human sperms over several hours, obtaining massive amounts of statistics about their 3D swimming patterns across 10–20 s for each continuous pattern. The large pool of statistics provided by this lensfree computational imaging platform enabled us to observe, for the first time, the helical trajectories of human sperms, exhibiting a tight helix radius of approximately 0.5–3 μm, a helical rotation speed of approximately 3–20 rotations/s and a linear speed of approximately 20–100 μm/s. Furthermore, this platform revealed that only approximately 4–5% of the motile human sperms swim along well-defined helices, and that this percentage of helical sperms can be considerably suppressed using seminal plasma. Quite interestingly, we also observed that a significant majority (approximately 90%) of these rare helical sperms preferred right-handed helices over left-handed ones, which is an observation that is enabled by the large spatial and temporal measurement windows that our on-chip imaging platform provides.

Compared to earlier reports that also used holographic imaging techniques (20–28) to track sperms or other microorganisms, our approach is lensfree (Fig. 1) and therefore exhibits a significantly larger imaging field-of-view of >17 mm^2 together with unit fringe magnification, while still achieving submicron positioning accuracy that is necessary to observe human sperms' tight helical paths. Furthermore, instead of using a laser source with high degree of coherence, we use partially-coherent illumination (both spatially and temporally) at two different wavelengths emanating from two light-emitting-diodes (LEDs) that are placed at 45° with respect to each other. This partially-coherent multiangle illumination at two different wavelengths (blue and red) significantly suppresses speckle and multiple-reflection interference noise terms as well as cross-interference among sperms' diffraction patterns, which make it feasible to track >1,500 sperms with submicron positioning accuracy. Our results on human sperms demonstrate the unique capabilities of this high-throughput on-chip imaging platform by resolving the tight and rapidly evolving rare helical trajectories of motile sperms. Finally, the same technique might in general be widely applicable for observing the statistical swimming patterns of various other microorganisms, leading to new insights in their 3D motion and the underlying biophysics.

Results

Human sperms exhibit a large variation in their 3D swimming patterns, and therefore using our dual-view lensfree holographic imaging platform (Fig. 1) we initially grouped these swimming patterns into four major categories as exemplified in Fig. 2 (typical, helical, hyperactivated, and hyperhelical; Table S1 and *Methods*). The "typical" trajectory shown in Fig. 2*A* (Movie S1)

Author contributions: T.-W.S. and A.O. designed research; T.-W.S., L.X., and A.O. performed research; T.-W.S. analyzed data; and T.-W.S. and A.O. wrote the paper.

The authors declare no conflict of interest.

This article is a PNAS Direct Submission. W.F.M. is a guest editor invited by the Editorial Board.

[1]To whom correspondence should be addressed. E-mail: ozcan@ucla.edu.

This article contains supporting information online at www.pnas.org/lookup/suppl/doi:10.1073/pnas.1212506109/-/DCSupplemental.

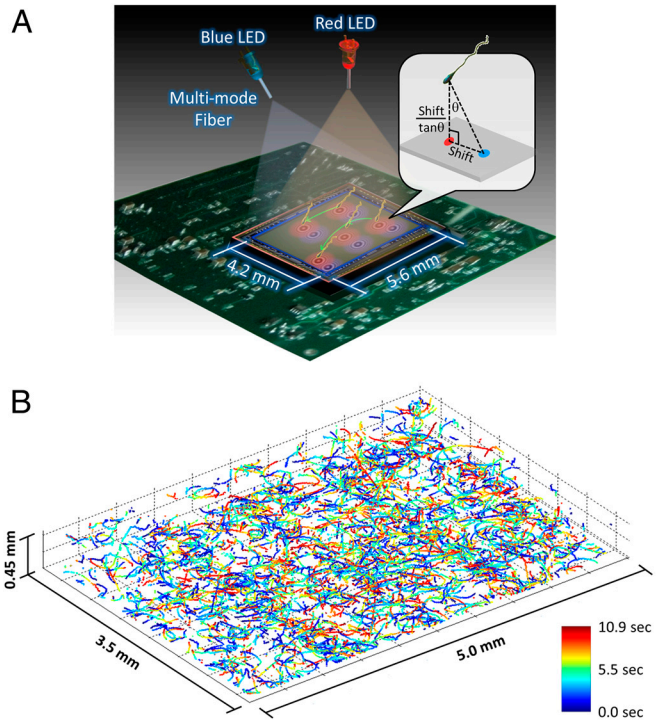

Fig. 1. Dual-view lensfree 3D tracking of human sperms. (*A*) The schematic diagram of the imaging system. Two partially-coherent light sources (red and blue LEDs at 625 nm and 470 nm, respectively) are butt-coupled to multimode fibers (0.4 mm core diameter each) to simultaneously illuminate the sperms at two different angles (red at 0° and blue at 45°). A CMOS sensor chip records the dual-view lensfree holograms that encode the position information of each sperm. The 3D location of each sperm is determined by the centroids of its head images reconstructed in the vertical (red) and oblique (blue) channels. This schematic diagram is not drawn to scale. (*B*) The reconstructed 3D sperm trajectories. 1,575 human sperms inside a volume of 7.9 μL were tracked at a frame rate of 92 FPS. The time position of each track point is encoded by its color (see the color bar).

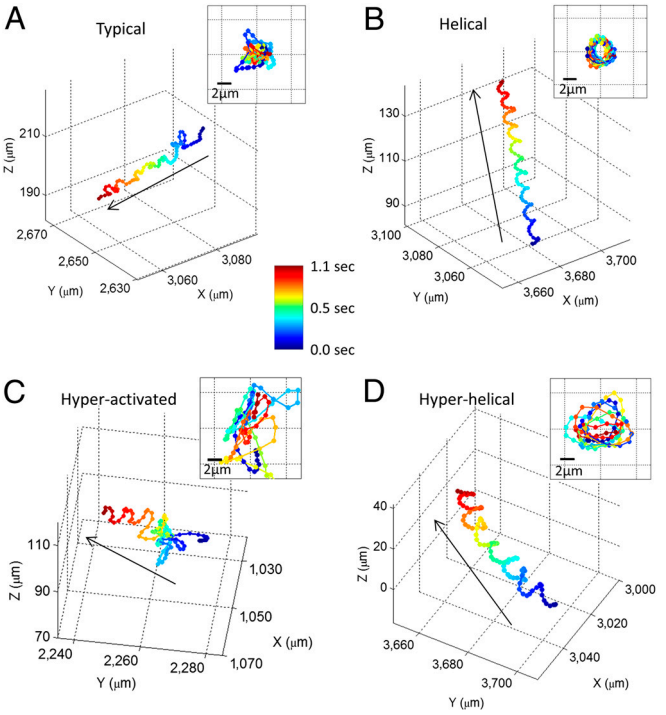

Fig. 2. Four major categories of human sperm swimming patterns. (*A*) The typical pattern. (*B*) The helical pattern. (*C*) The hyperactivated pattern. (*D*) The hyperhelical pattern. The inset in each panel represents the front view of the straightened trajectory of the sperm (*Methods*). The arrows indicate the directions of the sperms' forward movement. The time position of each track point is encoded by its color (see the color bar). The helices shown in (*B*) and (*D*) are both right-handed. See Movies S1–S4 for the time evolution of the sperm trajectories shown in (*A*–*D*), respectively. Some other examples of human sperm trajectories are also provided in Figs. S1–S4.

is the most prevalent swimming pattern observed among human sperms (>90%), in which the sperm head moves forward swiftly (as fast as 140 μm/s) along a slightly curved axis with a small lateral displacement (approximately 4 μm side-to-side). In this category (i.e., typical), although the lateral displacement exhibits a certain degree of periodicity, the sperm head changes its direction arbitrarily in 3D space (Fig. 2*A* and Fig. S1 *A*, *C*, and *D*). However, when these typical trajectories are located near the chamber boundaries, some of them also exhibit lateral displacements that are better confined to a two-dimensional plane, which is not necessarily parallel to the boundary (Fig. S1*B*).

In the second category of swimming patterns that human sperms exhibit, we observed helical trajectories (approximately 4–5% of motile human sperms, Table S1) as exemplified in Fig. 2*B* (Movie S2), which show the sperm head moving forward with very stable revolutions around a central axis, creating a well-defined helix. Not only is this helical trajectory (Fig. 2*B*) quite tight with an average helix radius of approximately 1.6 μm and a rotation speed of approximately 10 rotations/s, but also it moves rather fast, traveling more than 30–40 μm in depth-of-field (i.e., the *z* direction) within approximately 1 s, making it rather challenging to observe with a typical objective lens due to its limited depth-of-field and observation volume. In contrast to typical swimming patterns, we observed that the structure of these helical patterns did not alter much when the sperm head was near the boundaries of the observation chamber (Fig. S2).

In our third category, we observed hyperactivated 3D swimming patterns (<3% of motile human sperms, Table S1) that exhibit quite different movement compared to the previous two pattern types (Fig. 2*C* and Movie S3). The most noticeable change in a hyperactivated pattern is the decrease of its forward movement, despite the fact that the instantaneous speed of hyperactivated sperms (>150 μm/sec) is usually 2X faster than the instantaneous speed of typical or "helical" sperms. Most of the track length of a hyperactivated human sperm is consumed by the increased lateral movement, which has a size of >7 μm from one side to the other (Fig. 2*C*). This hyperactivated swimming pattern can be also divided into two subcategories, similar to 2D observations (5): (*i*) transitional hyperactivation, where the sperm still moves forward with a "meander" track (Fig. 2*C* and Fig. S3 *A* and *C*); and (*ii*) "star-spin" hyperactivation (mostly observed near the chamber boundaries), where the sperm bounces around vigorously but totally loses its forward movement as illustrated in Fig. S3*B*. Similar to the typical swimming patterns, many of the sperms in transitional hyperactivation category show quasi-2D lateral displacement near the chamber boundaries (compare Fig. S3 *A* and *C*, where the latter is much better confined to a plane).

In the final category of human sperm swimming patterns, we observed hyperhelical patterns (Fig. 2*D*, Fig. S3 *D*–*F*, and Movie S4), which can be considered as a combination of transitional hyperactivation and regular helical trajectories, exhibiting enlarged and slightly more unstable revolutions around a helix axis with a sustained forward movement. This swimming pattern was significantly rare, constituting only <0.5% of motile human sperms (Table S1). No major difference in swimming patterns was observed between the hyperhelical trajectories located in free 3D volume and the ones located near the chamber boundaries.

An important feature of the presented lensfree on-chip imaging approach is that it can track 3D trajectories of >1,500 human sperms over a large sample volume, which enables us

to observe the transitions among different swimming patterns across a time window of approximately 10–20 s for each continuous sperm trajectory. Fig. 3, Fig. S4, and Movie S5 illustrate some examples of such swimming pattern transitions acquired using our lensfree imaging platform. Based on our measurement results, Table S2 summarizes the statistics of such transitions among different swimming patterns observed in human semen samples. These results reveal that most of the observed helical and hyperactivated trajectories quickly switch back to typical swimming patterns (approximately 64% for helical trajectories and approximately 58% for hyperactivated trajectories).

Our human sperm tracking experiments can be further summarized in Fig. 4, where we quantify various parameters of 3D swimming patterns, curvilinear velocity (VCL), straight-line velocity (VSL), amplitude of lateral head displacement (ALH), beat-cross frequency (BCF), linearity (*SI Text*), and compare them to the statistical behavior of only the helical human sperms, which constitute <5% of the motile sperms. The mean values of these swimming parameters and their standard deviations are also listed in Tables S3 and S4. Based on these results, it is rather interesting to note that a significant majority (approximately 90%) of helical human sperms in baseline medium prefer right-handed helixes over left-handed ones (Fig. 4*F*), exhibiting a tight helix radius of 0.5–3 μm and a rotation speed of 3–20 revolutions/s.

To shed more light on this observation (i.e., the preference of right-handed helices), we performed an additional experiment (Fig. 5) to measure the percentage of helical trajectories as a function of time after the sperms were removed from seminal plasma and were placed into baseline medium (*SI Text*). The results of this time-traced experiment revealed that, after removal of the seminal plasma, the percentage of right-handed helical sperms significantly increased within approximately 2–3 h of incubation in baseline medium, reaching approximately 4–5% of motile human sperms (Fig. 5), which is also consistent with our previous observations in Fig. 4 and Table S1. On the other hand,

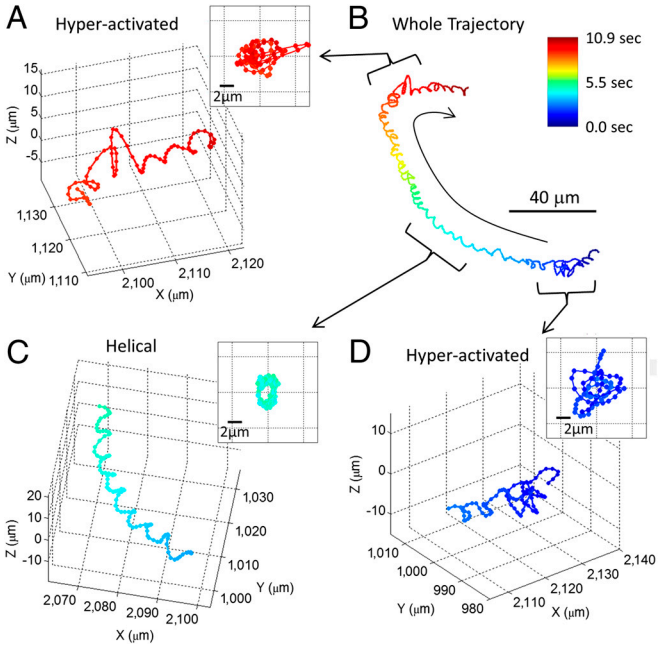

Fig. 3. A 10.9-s long trajectory showing the transitions between different swimming patterns of a human sperm. (*A*), (*C*), and (*D*) illustrate digitally extracted segments (approximately 1 s long each) of the whole sperm trajectory shown in (*B*). See Movie S5 for the time evolution of this trajectory. More sample trajectories with different pattern transitions are also provided in Fig. S4. The inset in each panel is the front view of the straightened trajectory of the sperm. The time position of each track point is encoded by its color (see the color bar).

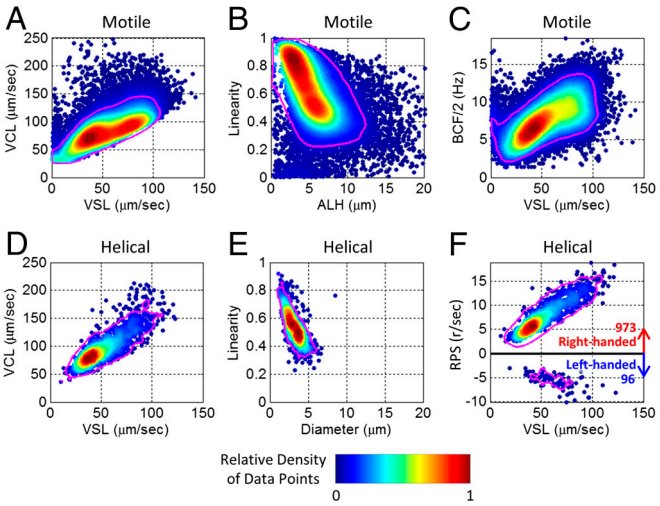

Fig. 4. Dynamic swimming parameters of 24,090 motile human sperms and 1,069 helical trajectories. Color bar represents the relative density of data points in each graph. Magenta lines enclose 90% of the motile/helical tracks presented in each panel. A helix with RPS > 0 (RPS < 0) is defined as right-handed (left-handed). VSL: straight-line velocity. VCL: curvilinear velocity. ALH: amplitude of lateral head displacement. BCF: beat-cross frequency. RPS: rotation speed. The unit r/s: revolutions per second. These measurements were made in baseline medium (artificial HTF) after >2 h of incubation as described in *SI Text*.

the same experiment did not reveal any major changes in the left-handed helical sperm percentage as a function of time, which remained to be <0.5% even after >3 h of incubation in baseline medium, as illustrated in Fig. 5.

These results also suggest that seminal plasma significantly suppresses helical trajectories of human sperms, while human tubal fluid initiates them. An experimental comparison of how different concentrations of seminal plasma affect the 3D swimming patterns of human sperms (in specific helical and hyperactivated trajectories) is also provided in Fig. 6, which once again confirmed the suppressing effect of seminal plasma on helical trajectories (after >2 h of incubation time, *SI Text*). Another important observation is that the helical trajectories, compared to the hyperactivated ones, were more difficult to suppress by increasing the percentage of seminal plasma in medium (Fig. 6), suggesting that these two swimming patterns might be regulated through different mechanisms.

Discussion

We should emphasize that to obtain large numbers of statistics regarding the swimming patterns of human sperms one would need a high-throughput imaging platform with submicron 3D tracking accuracy and sub-12-ms temporal resolution to clearly

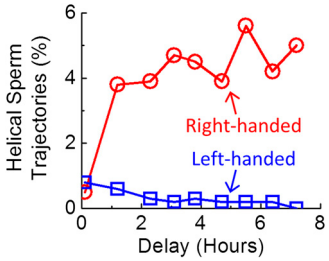

Fig. 5. Time evolution of helical sperm trajectories after resuspension in artificial human tubal fluid (HTF). After approximately 2–3 h of incubation in HTF, the percentage of right-handed helical trajectories significantly increased to approximately 4–5% of motile human sperms, while the percentage of left-handed ones did not show a major change, remaining <0.5% of motile sperms.

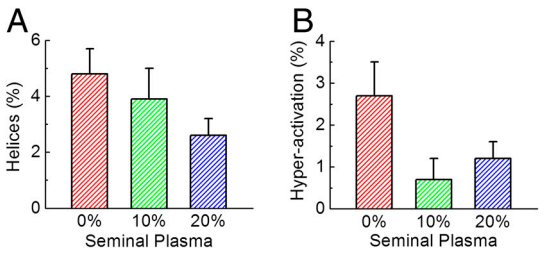

Fig. 6. Quenching of human sperms' helical (*A*) and hyperactivated (*B*) trajectories as a function of increased seminal plasma concentration in culture media. Each of the mean ± SD bars in (*A*) and (*B*) was based on 14 measurements of two specimens (seven with each) obtained from different anonymous donors.

resolve different patterns, especially the helical patterns, which exhibit a tight helix radius of approximately 0.5–3 μm with a fast rotation speed that might reach 15–20 rotations/s. Conventional microscopes equipped with high-magnification objective lenses and high-frame-rate cameras can only meet these requirements for imaging sperms along a 2D plane, which can infer limited information on their natural 3D motion (1–16). Estimation of the 3D trajectories of sperms from their 2D observations can also be feasible in some cases by assuming a known swimming pattern (15, 29). However, such approaches in general would not be able to infer the details and quantify the fine parameters of 3D sperm trajectories due to lack of position information along the third dimension. A 2D vs. 3D comparison of human sperm trajectories is provided in Fig. S5 to better illustrate that different swimming patterns of human sperms can look very similar in 2D observation while their 3D patterns are vastly different.

More advanced microscopy configurations (17–19) or holographic imaging schemes (20–28) have also been used to resolve 3D trajectories of sperms of other species. However, these previous approaches have not reported submicron 3D localization accuracy throughout a large observation volume of ≥1 μL. The dual-view partially-coherent holographic on-chip imaging technique described in this article uses a lensfree hologram recording configuration to image a large field-of-view of 17 mm^2 and utilizes a multicolor illumination scheme to achieve submicron localization accuracy for tracking human sperms within a volume of 8–17 μL. This high-throughput platform provides unique opportunities to observe the swimming patterns of human sperms and reveal their rare statistics for helical or hyperhelical trajectories, as summarized in *Results*.

In general, human sperm trajectories reconstructed by our 3D tracking technique are consistent with previous observations made by conventional lens-based 2D microscopy tools (1, 3–7, 12, 13). Most sperms swim forward with quasiperiodic small lateral displacements, while some sperms move with enlarged lateral displacement (transitional hyperactivation), and some other sperms display the "star-spin" movement (complete hyperactivation). In addition to this, the extra depth information provided by our lensfree imaging technique enabled us to reconstruct the complete 3D trajectories of human sperms, isolating the helical motion from planar or other types of swimming patterns.

Furthermore, our approach also permits investigation of sperms' 3D distribution inside an observation chamber, shedding more light on the effect of surface boundaries on 3D swimming patterns of human sperms. Similar to what was reported previously for chambers that are deeper than a sperm's body length (9, 30–33), we also observed the accumulation of human sperms on the inner surfaces of our observation chambers. Although such accumulation happens on both the top and bottom surfaces for all four swimming patterns (Fig. 2), the presence of the surface boundaries, as described in *Results*, only modifies the typical and hyperactivated patterns but not the helical ones. Note that in our experiments, we used plain glass surfaces without siliconization. With different surface treatment methods, our platform can also be used to study how the surface properties can affect the statistics of sperm movement.

Compared to the swimming patterns of sea urchin sperms, which have also been extensively studied (2, 8–11, 15–19, 29, 31, 34, 35), human sperms exhibit some distinct features in their 3D swimming behavior. First, motile human sperms, just like other mammalian sperms (36), occasionally display hyperactivated swimming patterns; however, sea urchin sperms do not exhibit hyperactivation. Second, when swimming near a surface, sea urchin sperms tend to follow circular swimming paths with a strongly preferred handedness (9, 11, 31, 34, 35), whereas human sperms do not exhibit such behavior. Third, helical trajectories of human sperms can be observed both in free 3D volume and near solid surfaces; however, sea urchin sperms only display helical movement in free 3D volume (17–19, 29). Fourth, the helical trajectories of human sperms, compared to sea urchin sperms (19), exhibit significantly smaller helix radii (1.6 ± 0.5 μm vs. 6.8 ± 1.1 μm) and faster rotation speeds (6.8 ± 4.6 r/s vs. 4.0 ± 0.8 r/s), making them much more challenging to resolve in 3D.

Although we have reported large statistics on 3D trajectories of >24,000 human sperms revealing several important observations that have so far been hidden due to limited capabilities of existing optical imaging platforms, most of the regulating mechanisms behind these observations still remain unclear. For example, in our experiments seminal plasma suppressed the percentage of helical sperm trajectories as illustrated in Fig. 6. This observation could be due to (*i*) the higher viscosity of seminal plasma; or (*ii*) its chemical composition. The effect of medium viscosity to make helical movement un-sustainable is also supported by previous studies, where high viscosity is shown to reduce the amplitude of sperms' lateral head displacement (12). However, the time lag (Fig. 5) between the removal of human sperms from seminal plasma and the appearance of helical trajectories suggests that there should be some other biochemical factors involved that delay the activation of this helical movement. By imaging human sperms in media with various activating or suppressing constituents, our 3D tracking platform can be used to better investigate the underlying mechanisms regulating such helical or hyperhelical patterns. Along the same lines, this lensfree sperm imaging platform can also provide a high-throughput tool to rapidly quantify the impact of various stimuli and drugs on the 3D swimming patterns of sperms.

Methods

3D Tracking of Human Sperms. The lensfree holographic frames recorded by the dual-view and dual-color lensfree holographic imaging setup (*SI Text*) were first individually reconstructed on all the possible object planes (with 25 μm vertical spacing) within the observation chamber, for both the vertical red illumination and the oblique blue illumination. This digital reconstruction process for each illumination wavelength follows the iterative phase recovery method that is detailed in our previous work (37). The digital separation of sperm head's vertical and oblique lensfree projections is discussed in *SI Text*, Fig. S6 and Movie S6. In each reconstructed lensfree frame, possible sperm candidates were segmented by thresholding the amplitude image for both color channels. Detection artifacts were filtered out with a series of morphological criteria, such as peak value, area, and eccentricity (38). Once confirmed as the projection of a sperm, the 2D centroid position of each sperm projection in both color channels was calculated by its center-of-gravity (38) based on the square of its reconstructed amplitude profile. At the same time, the focal distance of each vertical projection (which was estimated as the distance with the highest contrast in its reconstructed 2D image stack) was taken as the "coarse" vertical (i.e., *z*) distance of the sperm from the Complementary Metal—Oxide—Semiconductor sensor chip. This initial estimate has a lower depth accuracy of approximately 5–10 μm and is just used to search for the corresponding projection of each sperm in the oblique illumination channel. The 2D centroid position of the sperm head projection in the vertical channel was directly used as the sperm's *x*-*y* coordinate. The precise *z* coordinate of the sperm was then calculated by dividing the distance between its vertical and oblique projection centroids with the tangent

of the oblique illumination angle in water (Fig. 1*A*). Refer to *SI Text* and Fig. S7 for quantification of our submicron localization accuracy.

The same 3D localization procedures outlined above for human sperms were repeated for each recorded lensfree holographic frame to generate a 3D-t (i.e., space-time) matrix, which contains the spatial and temporal coordinates of all the sperm head positions detected in our observation volume. The trajectory of each sperm as a function of time was then constructed by linking up the nearest detected points (39) across the reconstructed 3D amplitude frames. To improve our tracking accuracy, we also used a Brownian-statistics-based algorithm (40) for better handling noise in our measurements.

Digital Classification of the Reconstructed Sperm Trajectories. The 3D swimming patterns of human sperms were categorized based on several dynamic parameters extracted from their reconstructed 3D-t trajectories, such as curvilinear velocity, linearity, lateral displacement, and number of stable turns (rotations) (*SI Text*). All the parameter extraction performed in this work was based on either 1.1 s-long trajectories (approximately 100 frames at 92 FPS) or track segments of such length that were digitally extracted from longer trajectories (10–20 s long).

Before automatically extracting these dynamic parameters for each sperm within our observation volume, the reconstructed 3D trajectory segments need to go through a digital "straightening" process to compensate the curvature in their 3D motion. To this end, a 3D parabolic curve model was used to fit the curved moving axis of each segment by minimizing the square of the distance between all the position points and the fitted axis (where the distance was created by the sperm's lateral displacement). All the position points were then reassigned laterally onto a plane moving along the axial direction according to their relative position to the fitted axis (Fig. S8 *A–C*). After this digital straightening step, the moving axis of each segment became a straight line and the position points evolved laterally around the fitted axis. The lateral coordinates of the position points (the X_r and Y_r in Fig. S8 *B* and *C*) were then used to calculate the instantaneous radius and the angle of the trajectory points (Fig. S8 *D* and *E*), where the instantaneous angle was further unwrapped to eliminate possible 2π phase jumps and fitted with a linear function to estimate its rotation speed.

Note that in this work we considered all the human sperm trajectories with a VCL that is smaller than 30 μm/s as immotile (41). The motile sperm trajectories that cannot be classified as helical, hyperactivated, or hyperhelical are then classified as typical trajectories. For distinguishing helical, hyperactivated and hyperhelical 3D sperm trajectories from typical ones, the following criteria have been used:

Helical trajectory—Number of stable turns, NST $\geq$ 2.0.
Hyperactivated trajectory—VCL needs to be larger than 150 μm/s; the linearity needs to be smaller than 0.5; and ALH needs to be larger than 7.0 μm.
Hyperhelical trajectory—All the requirements for both helical and hyperactivated trajectories need to be satisfied.

Because of the fact that the fitting of helices requires more than two stable turns and that the hyperactivated sperms can change their swimming patterns back and forth within a few seconds (5), longer sperm trajectories are digitally divided into track segments that are each approximately 1.1 s long, which is long enough for fitting a helix but short enough for minimizing swimming pattern transitions within each segment.

ACKNOWLEDGMENTS. We thank Drs. Christina Wang and Andrew Leung (Harbor-UCLA Medical Center, Torrance, CA, USA) for their valuable discussions and help on processing semen specimens. A.O. acknowledges the support of Army Research Office Young Investigator Award, National Science Foundation CAREER Award, the Office of Naval Research Young Investigator Award, and the National Institutes of Health Director's New Innovator Award DP2OD006427 from the Office of The Director, National Institutes of Health.

1. Phillips DM (1972) Comparative analysis of mammalian sperm motility. *J Cell Biol* 53:561–573.
2. Rikmenspoel R (1978) Movement of Sea Urchin Sperm Flagella. *J Cell Biol* 76:310–322.
3. Serres C, Feneux D, Jouannet P, David G (1984) Influence of the flagellar wave development and propagation on the human sperm movement in seminal plasma. *Gamete Res* 9:183–195.
4. Ishijima S, Oshio S, Mohri H (1986) Flagellar movement of human spermatozoa. *Gamete Res* 13:185–197.
5. Mortimer ST, Swan MA (1995) Variable kinematics of capacitating human spermatozoa. *Hum Reprod* 10:3178–3182.
6. Mortimer ST (2000) CASA—Practical aspects. *J Androl* 21:515–524.
7. Mortimer ST, Schëväert D, Swan MA, Mortimer D (1997) Quantitative observations of flagellar motility of capacitating human spermatozoa. *Hum Reprod* 12:1006–1012.
8. Woolley DM, Vernon GG (2001) A study of helical and planar waves on sea urchin sperm flagella, with a theory of how they are generated. *J Exp Biol* 204:1333–1345.
9. Woolley DM (2003) Motility of spermatozoa at surfaces. *Reprod* 126:259–270.
10. Kaupp UB, et al. (2003) The signal flow and motor response controling chemotaxis of sea urchin sperm. *Nat Cell Biol* 5:109–117.
11. Riedel IH, Kruse K, Howard J (2005) A self-organized vortex array of hydrodynamically entrained sperm cells. *Science* 309:300–303.
12. Smith DJ, Gaffney EA, Gadêlha H, Kapur N, Kirkman-Brown JC (2009) Bend propagation in the flagella of migrating human sperm, and its modulation by viscosity. *Cell Motil Cytoskeleton* 66:220–236.
13. Gillies EA, Cannon RM, Green RB, Pacey AA (2009) Hydrodynamic propulsion of human sperm. *J Fluid Mech* 625:445–474.
14. Friedrich BM, Riedel-Kruse IH, Howard J, Jülicher F (2010) High-precision tracking of sperm swimming fine structure provides strong test of resistive force theory. *J Exp Biol* 213:1226–1234.
15. Gurarie E, Grünbaum D, Nishizaki M (2011) Estimating 3D movements from 2D observations using a continuous model of helical swimming. *Bull Math Biol* 73:1358–1377.
16. Ishijima S (2012) Mechanical constraint converts planar waves into helices on tunicate and sea urchin sperm flagella. *Cell Struct Funct* 37:13–19.
17. Crenshaw HC (1996) A new look at locomotion in microorganisms: Rotating and translating. *Am Zool* 36:608–618.
18. Crenshaw HC, Ciampaglio CN, McHenry M (2000) Analysis of the three-dimensional trajectories of organisms: Estimates of velocity, curvature and torsion from positional information. *J Exp Biol* 203:961–982.
19. Corkidi G, Taboada B, Wood CD, Guerrero A, Darszon A (2008) Tracking sperm in three-dimensions. *Biochem Biophys Res Commun* 373:125–129.
20. Xu W, Jericho MH, Meinertzhagen IA, Kreuzer HJ (2001) Digital in-line holography for biological applications. *Proc Natl Acad Sci USA* 98:11301–11305.
21. Malkiel E, Sheng J, Katz J, Strickler JR (2003) The three-dimensional flow field generated by a feeding calanoid copepod measured using digital holography. *J Exp Biol* 206:3657–3666.
22. Jericho SK, Garcia-Sucerquia J, Xu W, Jericho MH, Kreuzer HJ (2006) Submersible digital in-line holographic microscope. *Rev Sci Instrum* 77:043706.
23. Lewis NI, et al. (2006) Swimming speed of three species of Alexandrium (Dinophyceae) as determined by digital in-line holography. *Phycologia* 45:61–70.
24. Heydt M, et al. (2007) Digital in-line holography as a three-dimensional tool to study motile marine organisms during their exploration of surfaces. *J Adhes* 83:417–430.
25. Sheng J, et al. (2007) Digital holographic microscopy reveals prey-induced changes in swimming behavior of predatory dinoflagellates. *Proc Natl Acad Sci USA* 104:17512–17517.
26. Frentz Z, Kuehn S, Hekstra D, Leibler S (2010) Microbial population dynamics by digital in-line holographic microscopy. *Rev Sci Instrum* 81:084301.
27. Sohn M, et al. (2011) Determination of the swimming trajectory and speed of chain-forming dinoflagellate Cochlodinium polykrikoides with digital holographic particle tracking velocimetry. *Mar Biol* 158:561–570.
28. Lee SJ, Seo KW, Choi YS, Sohn MH (2011) Three-dimensional motion measurements of free-swimming microorganisms using digital holographic microscopy. *Meas Sci Technol* 22:064004.
29. Guerrero A, et al. (2011) Strategies for locating the female gamete: The importance of measuring sperm trajectories in three spatial dimensions. *Mol Hum Reprod* 17:511–523.
30. Winet H, Bernstein GS, Head J (1984) Observations on the response of human spermatozoa to gravity, boundaries and fluid shear. *J Reprod Fertil* 70:511–523.
31. Cosson J, Huitorel P, Gagnon C (2003) How spermatozoa come to be confined to surfaces. *Cell Motil Cytoskeleton* 54:56–63.
32. Smith DJ, Gaffney EA, Blake JR, Kirkman-Brown JC (2009) Human sperm accumulation near surfaces: A simulation study. *J Fluid Mech* 621:289–320.
33. Elgeti J, Kaupp UB, Gompper G (2010) Hydrodynamics of sperm cells near surfaces. *Biophys J* 99:1018–1026.
34. Ishijima S, Hamaguchi Y (1992) Relationship between direction of rolling and yawing of golden hamster and sea urchin spermatozoa. *Cell Struct Funct* 17:319–323.
35. Ishijima S, Hamaguchi Y (1993) Calcium ion regulation of chirality of beating flagellum of reactivated sea urchin spermatozoa. *Biophys J* 65:1445–1448.
36. Ho HC, Suarez SS (2001) Hyperactivation of mammalian spermatozoa: Function and regulation. *Reprod* 122:519–526.
37. Isikman SO, et al. (2011) Lens-free optical tomographic microscope with a large imaging volume on a chip. *Proc Natl Acad Sci USA*, Available at: http://www.pnas.org/content/early/2011/04/15/1015638108.abstract [Accessed December 4, 2011].
38. Su T-W, et al. (2010) Multi-angle lensless digital holography for depth resolved imaging on a chip. *Opt Express* 18:9690–9711.
39. Su T-W, Erlinger A, Tseng D, Ozcan A (2010) Compact and light-weight automated semen analysis platform using lensfree on-chip microscopy. *Anal Chem* 82:8307–8312.
40. Crocker JC, Grier DG (1996) Methods of digital video microscopy for colloidal studies. *J Colloid Interface Sci* 179:298–310.
41. World Health Organization (1999) *WHO Laboratory Manual for the Examination of Human Semen and Sperm-Cervical Mucus Interaction* (Cambridge University Press, Cambridge, UK), 4th Ed.

Supporting Information

Su et al. 10.1073/pnas.1212506109

SI Text

SI Methods. ***Preparing and incubating human sperm suspension.*** Fresh semen specimens within less than 1 h after collection (from anonymous donors) were obtained from California Cryobank without preprocessing. Only specimens with high sperm concentration ($>50 \times 10^6$ sperms per mL) and high motility (>70% motile) were used in our experiments. The motile sperms were first separated from seminal plasma by centrifugation with density gradient media (ISolate, Irvine Scientific) and then washed twice with artificial human tubal fluid (HTF, Sperm Washing Medium, Irvine Scientific) to completely remove the residue of seminal plasma. After the second washing step, the sperms were resuspended with various culture media in centrifuge tubes at a concentration of approximately 10×10^6 sperms per mL and incubated at 37 °C with pH buffer Hepes until our imaging measurements. Three different culture media were used in this work: *(i)* Baseline medium, which only contained artificial HTF; *(ii)* suppressing medium I, which was prepared by mixing seminal plasma with HTF by a ratio of 1:9; and *(iii)* suppressing medium II, which was prepared by mixing seminal plasma with HTF by a higher ratio of 2:8. For all our imaging experiments except the time-traced ones (e.g., Fig. 5), the sperm suspensions were incubated for approximately 2–3 h. Right before lensfree imaging experiments, approximately 50–150 μL of the sperm suspension was put into a disposable observation chamber prepared by taping a laser-cut Acetal film (approximately 0.1–0.5 mm thick) between two pieces of No. 1 cover slips.

Dual-view and dual-color lensfree holographic imaging setup. The configuration of our imaging setup is illustrated in Fig. 1*A*. The observation chamber containing the sperm suspension is placed directly on top of the protective glass of a Complementary Metal—Oxide—Semiconductor (CMOS) image sensor (Aptina MT9P031STC, 5 megapixels, 2.2 μm pixel size, monochrome) creating a physical distance of approximately 0.8 mm between the bottom of the chamber and the top surface of the CMOS sensor active area. The sample suspension is simultaneously illuminated by two partially-coherent light sources with different central wavelengths placed at 45° with respect to each other (vertical one: 625 nm; oblique one at 45°: 470 nm). Both light sources were composed of light-emitting-diodes (LEDs, bandwidth approximately 20 nm) that were simply butt-coupled to multimode optical fibers (core size: 0.4 mm) with the fiber tips placed at a distance of approximately 10 cm from the sample chamber. Such a system, without utilizing any lenses or mechanical scanners, can simultaneously record in-line holograms of the sperms from two different viewing angles over a large field-of-view, e.g., >20 mm^2, while also significantly reducing unwanted noise terms such as speckle patterns, multiple reflection interference noise or cross-interference among sperms' holograms (1, 2). To capture the dynamics of the sperms with minimum motion blur, the electronic shutter of the CMOS image sensor was set to 5 ms for defining the integration time of each pixel. The FOV of the CMOS imaging platform (i.e., 24 mm^2) was digitally programmed into 16 regions-of-interest (ROIs), which were sequentially recorded at a frame rate of 92 frames per second (FPS) for continuous intervals of approximately 1–20 s each. The resulting video data were transmitted to a PC in real time through a gigabit Ethernet connection. To avoid the heating of the image sensor between tracking experiments, which might damage the sperms inside the observation chamber, a programmable power relay (connected to the PC through a USB interface) was used to cut off the power of the image sensor between video acquisitions. The ON-OFF cycle of the image sensor was carefully configured to maintain the observation chamber at 36–37 °C for several hours. A custom-designed LabVIEW program was used to coordinate the image sensor and the power relay for maintaining the temperature as well as to digitally scan over the 16 ROIs of the observation chamber. Scanning over 16 ROIs (with >1,600 lensfree holograms) and recording the trajectories of >1,500 sperms takes approximately 10 min for each semen sample. However, this acquisition time can be significantly reduced to approximately 30 s if external cooling is provided to prevent the overheating of the observation chamber.

Digital separation of sperm head's vertical and oblique lensfree projections. Because the spatial information of each sperm was encoded with different wavelengths at two viewing angles, only the reconstruction that is performed with the correct combination of distance (i.e., depth), angle, and wavelength can generate clear images of the sperms (Fig. S6). Since incorrectly reconstructed projection holograms of the sperms would only show up as weak background noise, the sperm head images projected in two different viewing angles at two different wavelengths can be isolated from each other although they were recorded at the same lensfree holographic frame. This provides an important solution to avoid confusing different projections of different sperms with each other, especially at high sperm densities, making our 3D tracking algorithm quite robust. Furthermore, without the need to record different viewing angles separately, this multicolor approach also simplifies our system, eliminating the use of pulsed light sources, high-speed digital cameras, and the synchronization between them.

We should also emphasize that the swimming sperm tails do not constitute a problem in our localization calculations since they are considerably narrower (≤0.6 μm) compared to the sperm head (approximately 3–4 μm wide) and exhibit very weak light scattering (3), which significantly decreases their holograms' strength compared to the sperm heads' holograms. This behavior is also confirmed by the fact that the swimming sperm tails do not appear in the reconstructed amplitude images of our lensfree system (Fig. S6).

Quantification of submicron 3D localization accuracy. Since the centroid coordinates of the vertical and oblique projections can be determined with an accuracy much better than the 2.2-μm CMOS pixel size (4), the dual-view holographic approach use can localize individual sperms in 3D with submicron accuracy. To shed more light on this, we conducted characterization experiments with 3 μm particles that are spread across flat glass surfaces, and the results of these experiments confirmed that we can provide a 3D localization accuracy of approximately 0.3–0.5 μm across a depth-of-field of approximately 2.7 mm (Fig. S7). Note that at larger depths (>3 mm) the signal-to-noise ratio of lensfree holograms relatively degrades, reducing our 3D localization accuracy. We chose 3 μm particles in these characterization experiments since they exhibit a contrast that is matched to human sperms in our reconstructed amplitude images.

Definitions of human sperm's 3D dynamic parameters. To quantify the 3D trajectories of human sperms with parameters that are compatible with the currently existing standards, we appropriately modified the parameters that are used by computer-aided

sperm analysis (CASA) systems (5), which can be summarized as below:

i. *Straight-line velocity* (VSL) is defined as the distance between the first and the last position points in the track segment of a sperm trajectory divided by the total duration of the track segment (unit: μm/sec).
ii. *Curvilinear velocity* (VCL) is defined as the sum of the distances between every two consecutive position points in a track segment divided by the total duration of the track segment (unit: μm/sec).
iii. *Linearity* is the ratio between straight-line velocity and curvilinear velocity (VSL/VCL) of a track segment (unit: none).
iv. *Amplitude of lateral head displacement* (ALH) is defined as twice the maximum displacement of a sperm head from its fitted moving axis in a track segment (unit: μm). It is directly related to the level of bending in the proximal region of the tail (6) (i.e., a larger ALH value corresponds to stronger bending).
v. *Beat-cross frequency* (BCF) is defined as the frequency that the sperm head moves across the middle plane of the "straightened" trajectory (unit: Hz). The middle plane is determined as the plane in the X_r-Y_r-Z_{ax} space that contains the central axis Z_{ax} and has the most frequent crossing-over of the sperm head (Fig. S8*C*). The value of BCF is in general sublinearly proportional to the beating frequency of the sperm tail and is roughly double the frequency of head wobbling (7).
vi. *Rotation speed* (RPS) is defined as the slope of the linear function that best fits the time evolution of the unwrapped rotation angle of a sperm head projected on the X_r-Y_r plane (unit: revolutions per second, r/sec). It represents how fast a helical track segment revolves around its moving axis and is roughly half of the value of the trajectory's beat–cross frequency.
vii. *Number of stable turns* (NST) is defined by multiplying the rotation speed of a sperm with the duration that a track segment maintains a small error (≤0.6 radians in this study) to the fitted linear function in its unwrapped angle (Fig. S8*E*); unit: none. The segment with a small angle error needs to be longer than one rotation cycle for being counted into the number of stable turns. NST represents how close the track segment is to a bended helix and we chose a value equal to or larger than 2 to qualify this track segment as a "helical sperm trajectory" (Fig. S2).

Automated processing of 3D sperm trajectory data. Data processing procedures including reconstruction of lensfree holographic images, localization of sperms' 3D centroids, tracking sperms' motion, and classification of their 3D swimming patterns were performed fully-automated with custom-designed Matlab programs. The typical computation time for automatic processing of, e.g., approximately 1,600 lensfree images from a single semen sample is approximately 2.2 h (using Matlab R2011a running on a PC with an eight-core Intel Core i7-930 2.80 GHz processor). Since most of these procedures are highly repetitive and parallelizable, this computation time can be significantly shortened (by >5-10X) (8) once our algorithms are further optimized for execution on graphics processing units (GPUs).

1. Mudanyali O, et al. (2010) Compact, light-weight and cost-effective microscope based on lensless incoherent holography for telemedicine applications. *Lab Chip* 10:1417–1428.
2. Greenbaum A, Sikora U, Ozcan A (2012) Field-portable wide-field microscopy of dense samples using multiheight pixel super-resolution based lensfree imaging. *Lab Chip* 12:1242–1245.
3. Su T-W, Erlinger A, Tseng D, Ozcan A (2010) Compact and light-weight automated semen analysis platform using lensfree on-chip microscopy. *Anal Chem* 82:8307–8312.
4. Su T-W, et al. (2010) Multiangle lensless digital holography for depth resolved imaging on a chip. *Opt Express* 18:9690–9711.
5. Mortimer ST (2000) CASA—Practical aspects. *J Androl* 21:515–524.
6. Mortimer ST, Schëväert D, Swan MA, Mortimer D (1997) Quantitative observations of flagellar motility of capacitating human spermatozoa. *Hum Reprod* 12:1006–1012.
7. Serres C, Feneux D, Jouannet P, David G (1984) Influence of the flagellar wave development and propagation on the human sperm movement in seminal plasma. *Gamete Res* 9:183–195.
8. Herraiz JL, et al. (2009) GPU acceleration of a fully 3D Iterative Reconstruction Software for PET. *2009 IEEE Nuclear Science Symposium Conference Record (NSS/MIC)* (IEEE), pp 4064–4067.

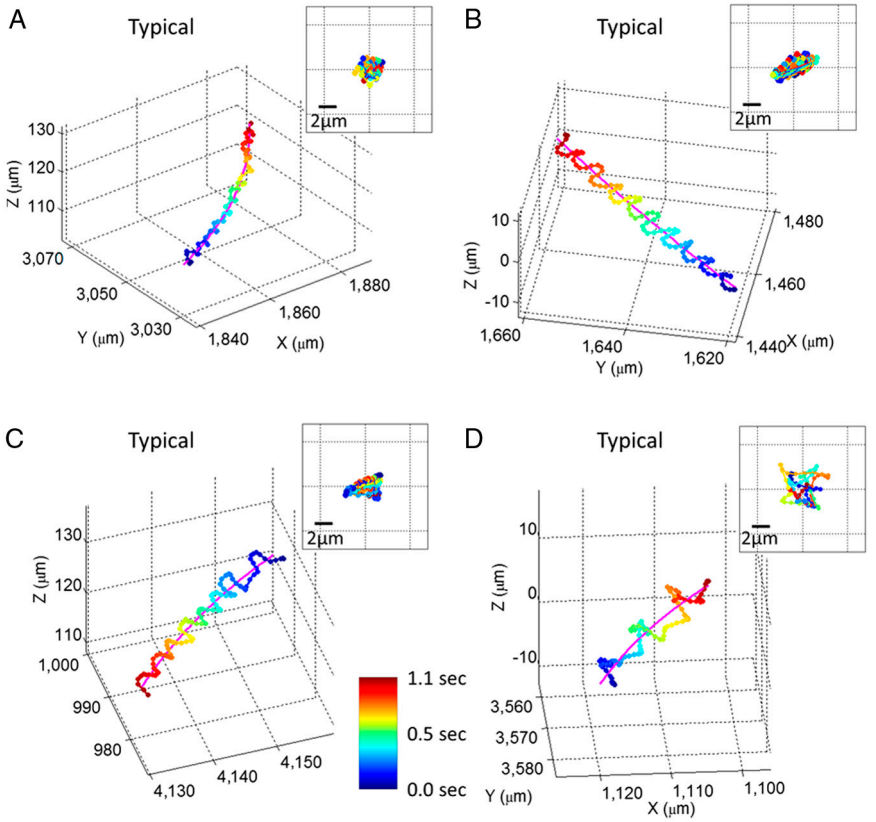

Fig. S1. Additional examples of human sperm typical swimming patterns. The inset in each panel is the front-view of the straightened trajectory of the sperm. The plane of $Z = 0$ is roughly aligned with the *Bottom* of the observation chamber. The time position of each track point is encoded by its color (see the color bar).

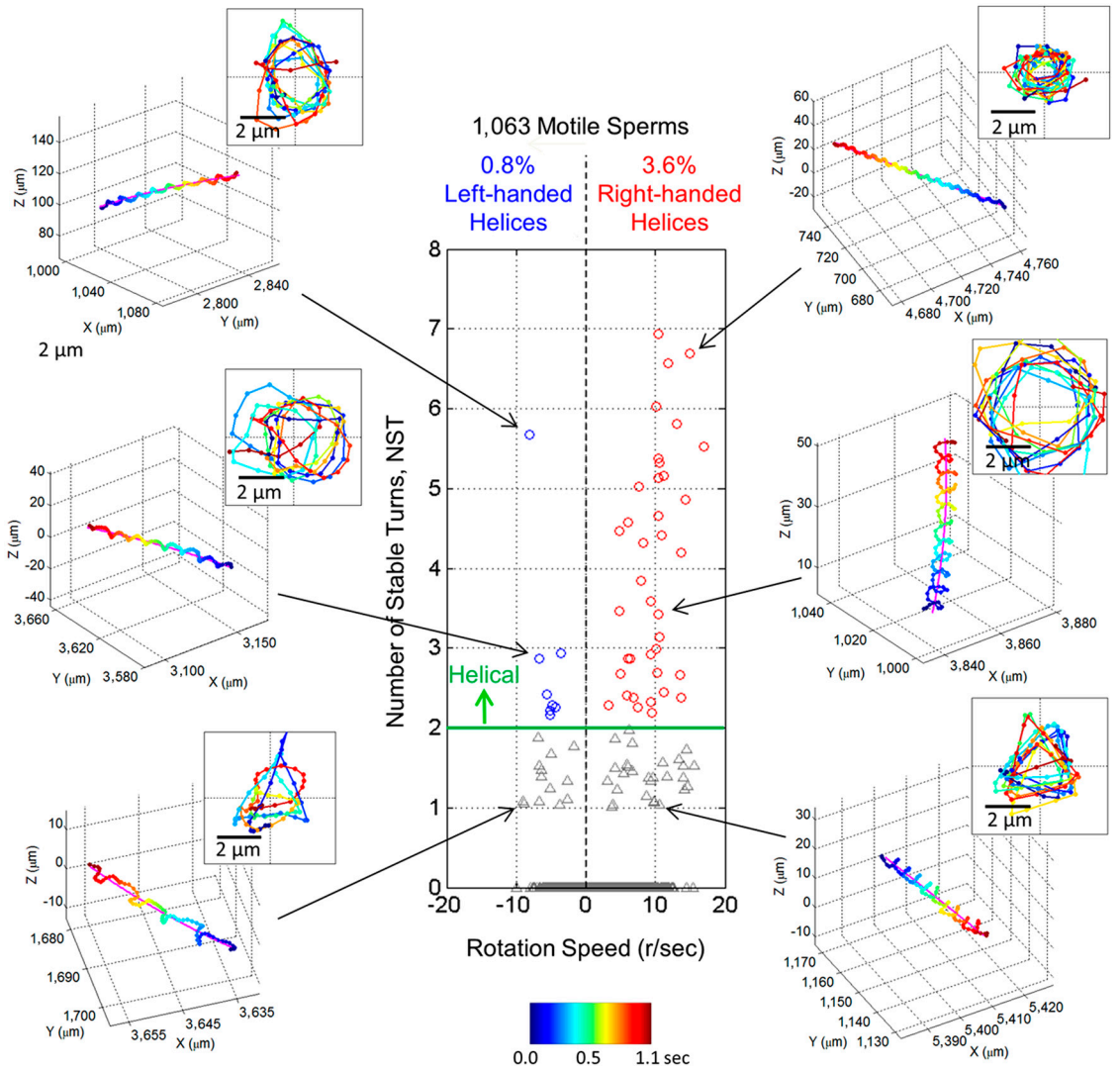

Fig. S2. Various examples of human sperm helical trajectories with different NST values. Within a given track period of approximately 1.1 s, a trajectory with more than two stable turns (NST $\geq$ 2.0) is considered a helical one (*Methods*). The plane of $Z = 0$ is roughly aligned with the *Bottom* of the observation chamber. The time position of each track point is encoded by its color (see the color bar).

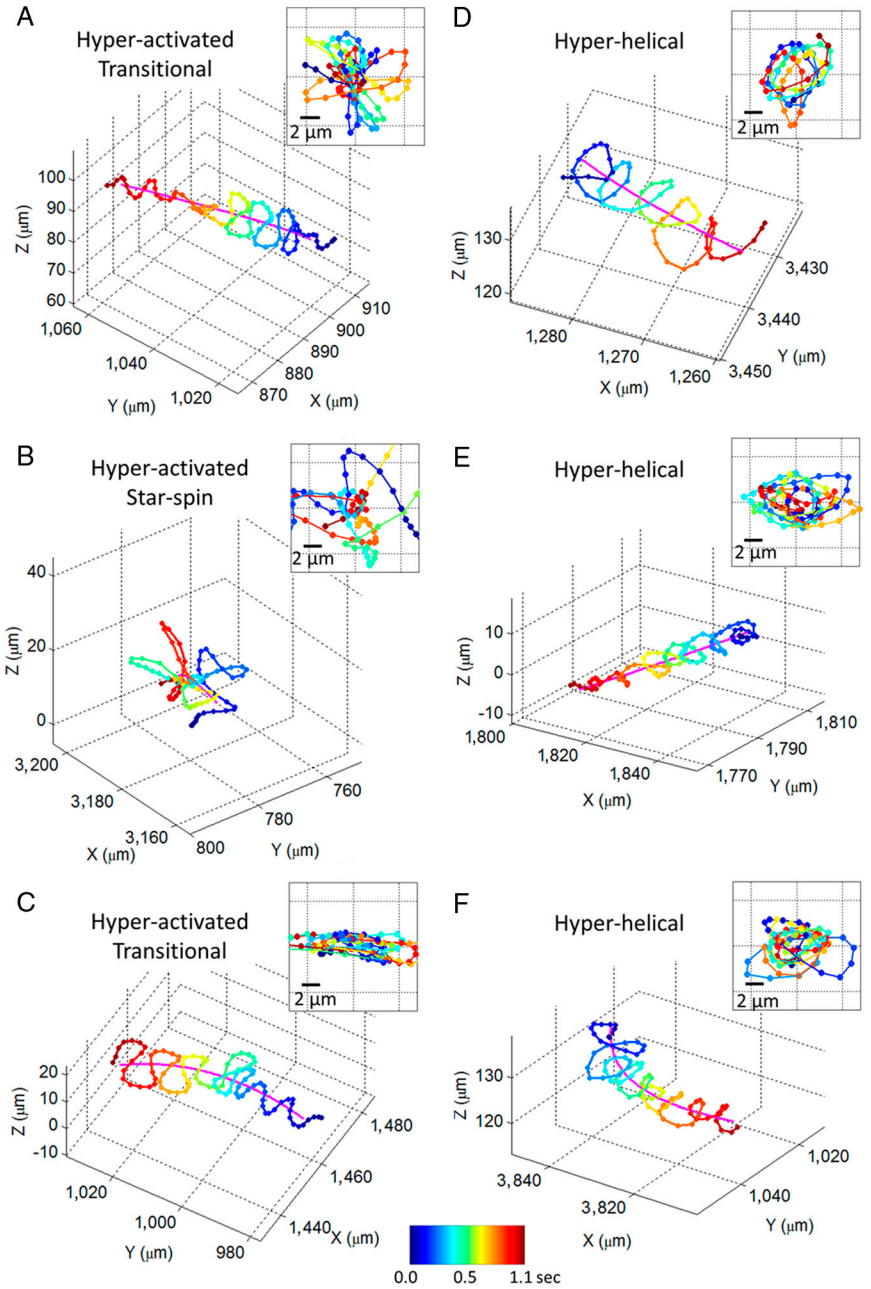

Fig. S3. Additional examples of hyperactivated (*A–C*) and hyperhelical (*D–F*) trajectories of human sperms. The inset in each panel is the front-view of the straightened trajectory of the sperm. The plane of $Z = 0$ is roughly aligned with the *Bottom* of the observation chamber. The time position of each track point is encoded by its color (see the color bar).

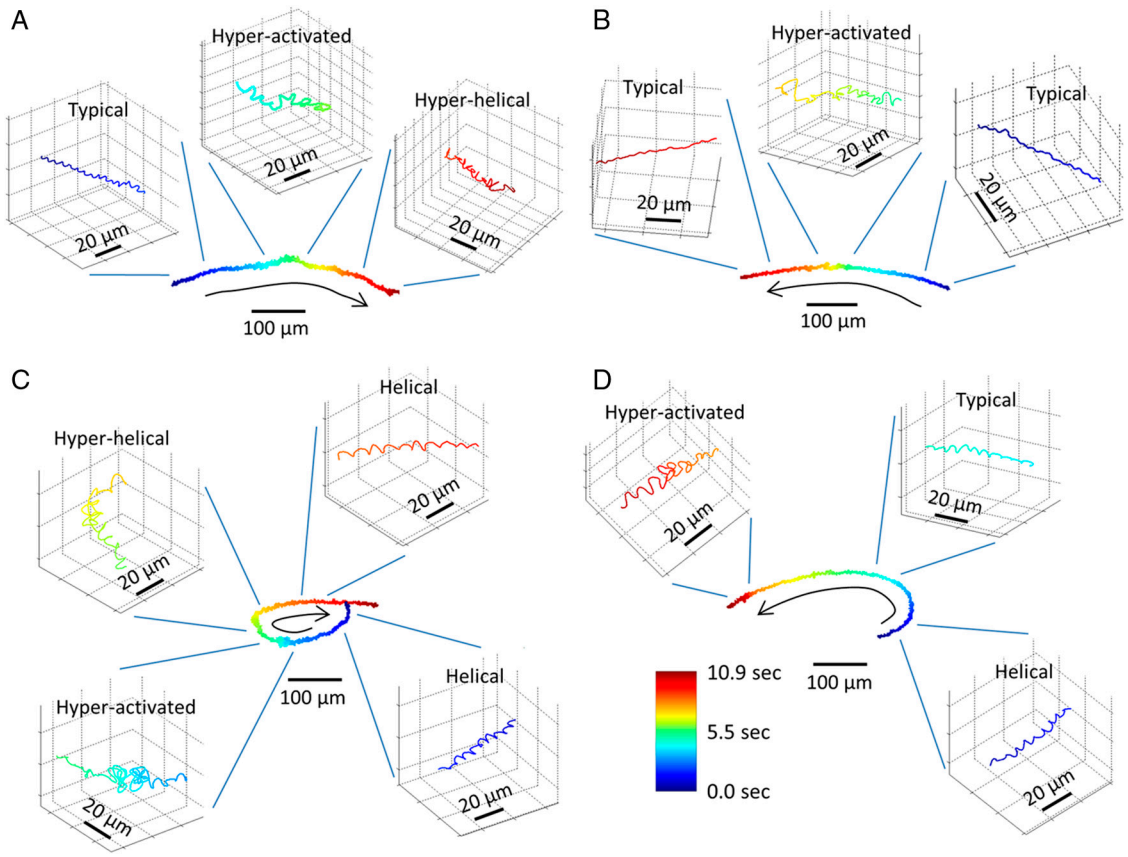

Fig. S4. Additional examples of human sperm trajectories showing the transitions among different 3D swimming patterns. The whole trajectories shown in (*A*), (*B*), (*C*), and (*D*) are each 10.9 s long, and the insets are digitally extracted segments of approximately 1.1 s. The time position of each track point is encoded by its color (see the color bar).

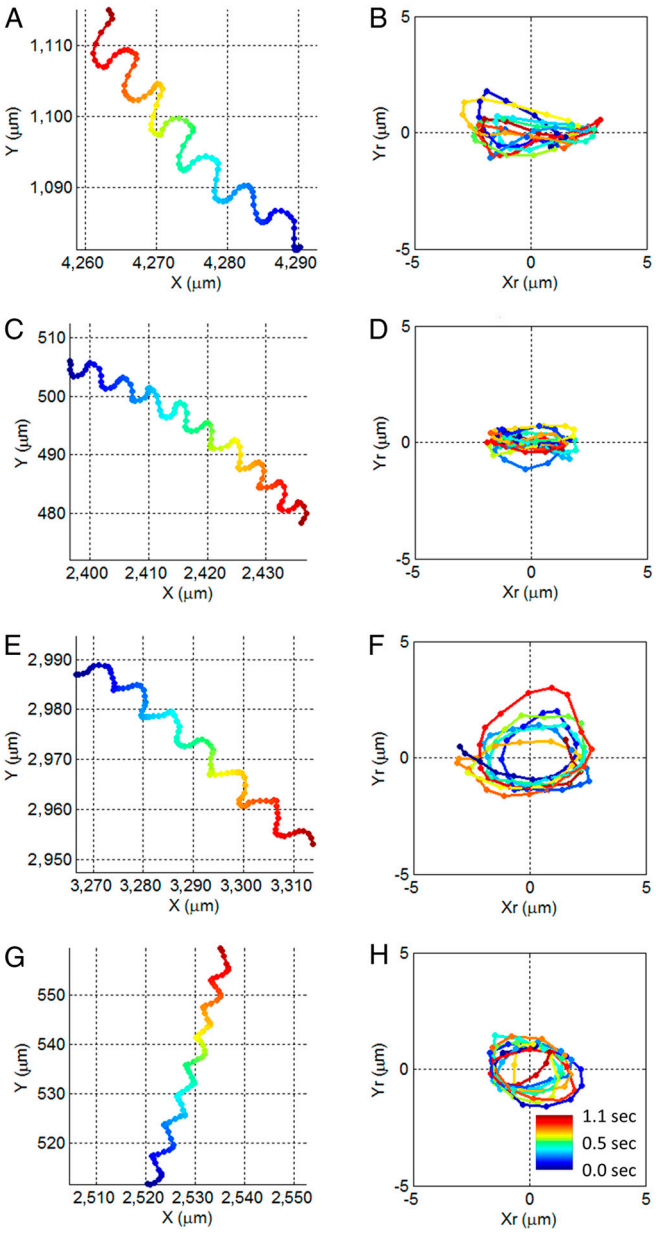

Fig. S5. 2D vs. 3D tracking of human sperms. (*A*) and (*C*) 2D tracking of two planar sperm trajectories. (*B*) and (*D*) The front views of the straightened 3D trajectories for (*A*) and (*C*), respectively (Fig. S8 and *SI Methods*). (*E*) and (*G*) 2D tracking of two helical sperm trajectories. (*F*) and (*H*) The front views of the straightened 3D trajectories for (*E*) and (*G*), respectively. As illustrated in this figure, unlike 3D imaging, 2D tracking of human sperms cannot differentiate planar and helical trajectories from each other.

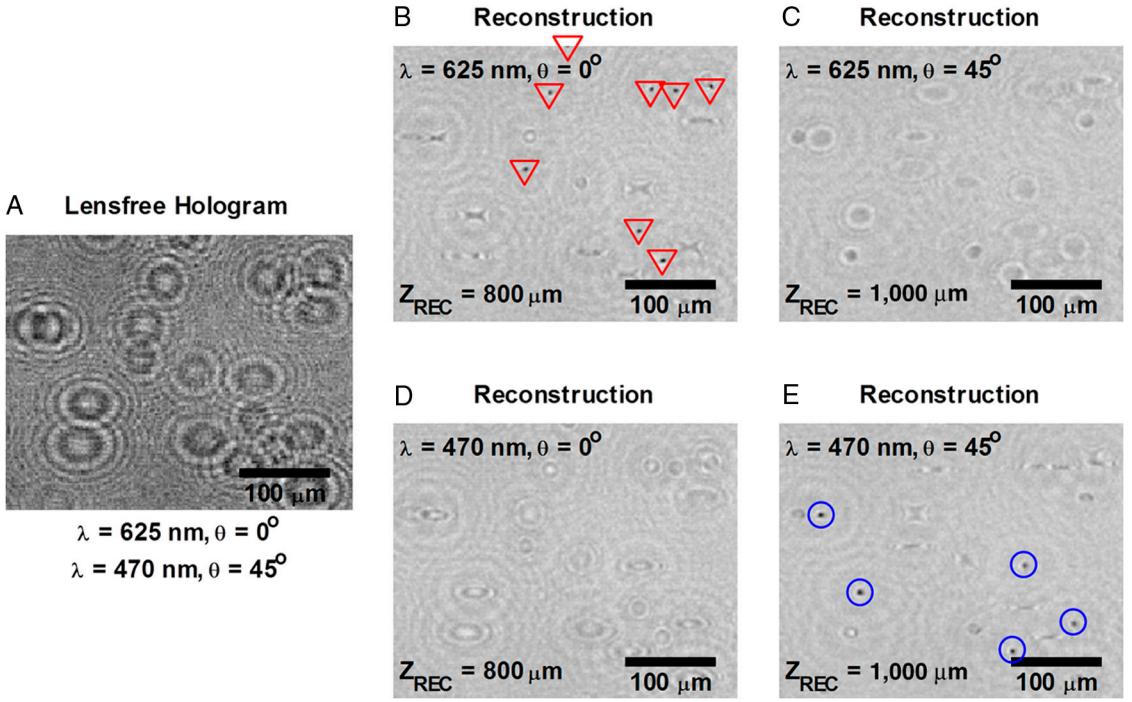

Fig. S6. Digital separation of the sperms' vertical and oblique lensfree projections through dual-angle and dual-color partially-coherent illumination. (*A*) A lensfree image showing several sperm holograms recorded with a red LED at the vertical angle and a blue LED at the oblique angle simultaneously illuminating the sample. (*B*)–(*E*) Lensfree images that were digitally reconstructed from the same region of interest shown in (*A*), but each with the conditions specified in its legends. The red triangles in (*B*) mark the successful detection of the vertical projections of the sperms, whereas the blue circles in (*E*) label the successful detection of oblique projections. Reconstruction with parameters that are not matched to the original illumination conditions would only create weak noise at the background as illustrated in (*C*–*D*). See Movie S6 for the time evolution of this lensfree hologram and its reconstruction images.

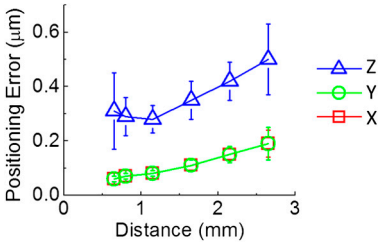

Fig. S7. The localization accuracy of the lensfree 3D tracking system as a function of the vertical distance from the sensor surface. The positional error was characterized by tracking microparticles (diameter: 3 μm) that are spread across flat glass surfaces and calculating the standard deviation of 3D positions for individual stationary particles. The vertical distance is defined by the separation between the localized object and the imaging plane of the CMOS sensor, which was adjusted by inserting glass slides of different thicknesses. Error bars define SD.

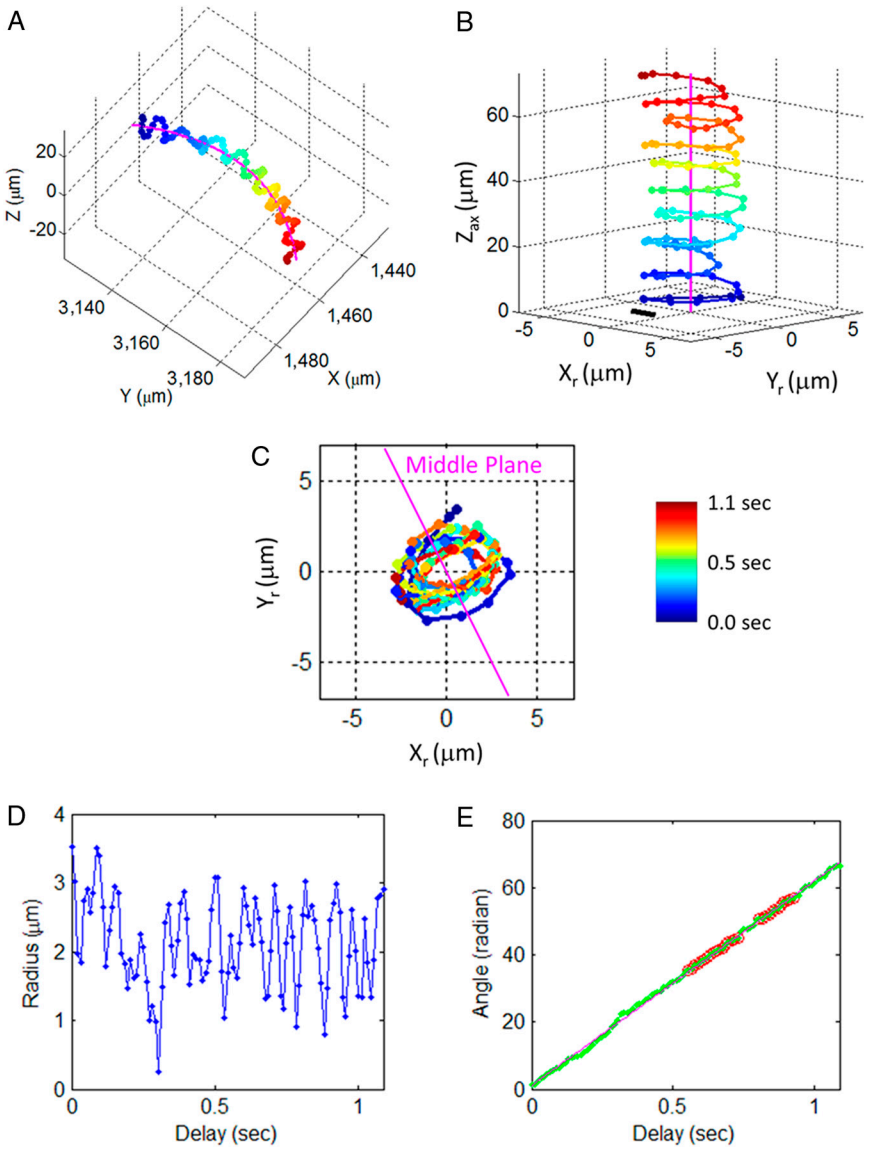

Fig. S8. Detection of a helical trajectory for a human sperm. (*A*) The original human sperm helix fitted with a parabolic line (magenta color) as its curved axis. (*B*) The same helix is straightened by replacing each point along a straight axis according to its relative displacement to the fitted axis (the magenta line). (*C*) The front view of the straightened helix shown in (*B*). The magenta line marks the middle plane that is used to measure the beat-cross frequency (*SI Methods*). The instantaneous radius (*D*) and angle (*E*) extracted from the lateral coordinates (i.e., X_r and Y_r) of the helix shown in (*C*). The angle in (*E*) is first unwrapped to eliminate possible 2π phase jumps and then fitted with a linear function (the magenta line) to match a stable rotation. Red circles on the magenta line in (*E*) mark the angular data points (the green dots) that lie within ± 0.6 radians from the fitted linear function.

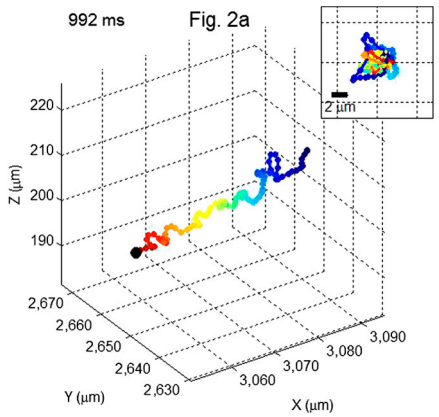

Movie S1. An example of human sperm typical swimming pattern.
Movie S1 (AVI)

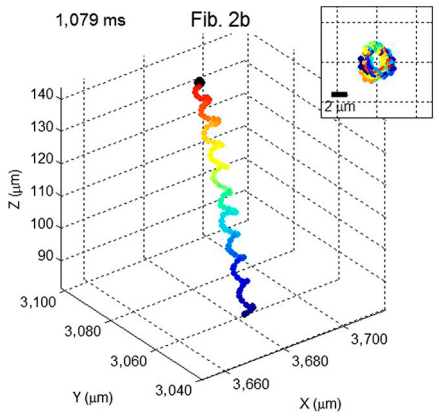

Movie S2. An example of human sperm helical swimming pattern.
Movie S2 (AVI)

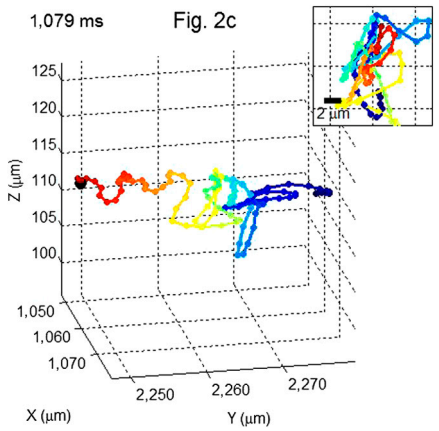

Movie S3. An example of human sperm hyperactivated swimming pattern.
Movie S3 (AVI)

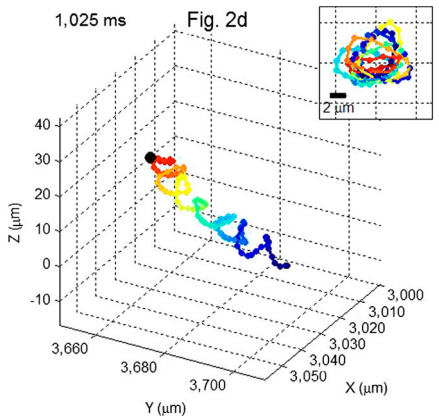

Movie S4. An example of human sperm hyperhelical swimming pattern.
Movie S4 (AVI)

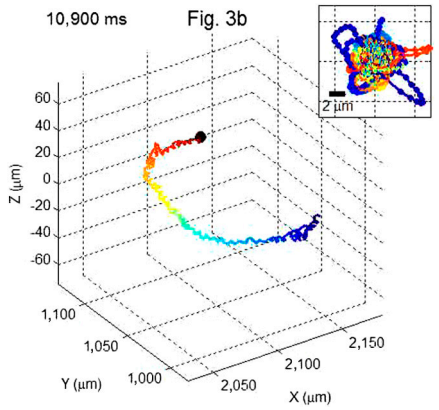

Movie S5. A 10.9-s-long trajectory showing the transitions between different swimming patterns of a human sperm.
Movie S5 (AVI)

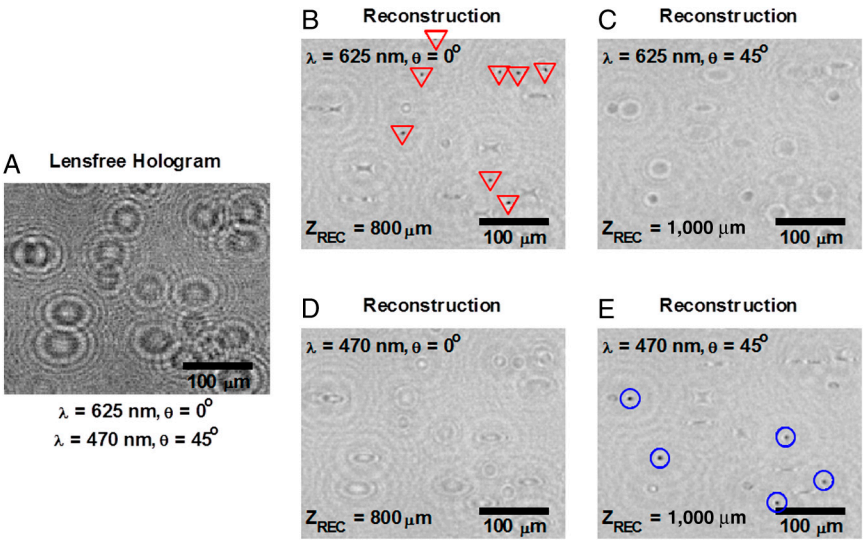

Movie S6. Digital separation of the sperms' vertical and oblique projections.
Movie S6 (AVI)

Table S1. The relative ratios of different swimming patterns

	Typical	Helical	Hyperactivated	Hyperhelical
Mean	**92.9%**	**4.4%**	**2.5%**	**0.2%**
Standard Deviation	(± 5.3%)	(± 1.5%)	(± 1.3%)	(± 0.2%)

These patterns were observed in 28 measurements of six semen specimens from different donors, containing 24,090 motile human sperms. The standard deviations listed in parentheses were obtained by calculating the deviation of each ratio observed across all the 28 measurements. These measurements were made in baseline medium (artificial HTF) after >2 h of incubation as described in *SI Methods*.

Table S2. The relative percentage of swimming pattern transitions (*From–To*)

		To			
		Typical	Helical	Hyperactivated	Hyperhelical
From	Typical	**85.1%** (± 8.1%)	**10.1%** (± 7.0%)	**4.8%** (± 4.1%)	**0.0%** (± 0.0%)
	Helical	**63.8%** (± 25.0%)	**30.0%** (± 22.1%)	**5.0%** (± 10.3%)	**1.3%** (± 3.6%)
	Hyperactivated	**57.7%** (± 31.3%)	**2.1%** (± 4.7%)	**30.9%** (± 28.6%)	**9.3%** (± 9.2%)
	Hyperhelical	**36.7%** (± 38.5%)	**13.3%** (± 30.7%)	**40.0%** (± 44.9%)	**10.0%** (± 30.3%)

The relative percentage of swimming pattern transitions (*From–To*) observed within 3,473 segments (each approximately 1.1 s long) of 656 human sperms trajectories (each approximately 5.5–10.9 s long). The standard deviations in parentheses were obtained by randomly dividing the 656 trajectories into 16 groups and calculating the relative percentage deviation of each transition across these groups.

Table S3. Typical values of various dynamic swimming parameters measured for motile human sperms

	Straight-line velocity (VSL) (μm/sec)	Curvilinear velocity (VCL) (μm/sec)	Linearity (VSL/VCL)	Lateral head displacement (ALH) (μm)	Beat-cross frequency (BCF) (Hz)
Mean	55.7	88.0	0.61	5.4	15.7
Standard Deviation	(± 24.9)	(± 28.7)	(± 0.21)	(± 2.9)	(± 5.1)

This table shares the same data as in Fig. 4 *A*, *B*, and *C* of the main text.

Table S4. Typical values of various dynamic swimming parameters measured for helical trajectories of human sperms

	Straight-line velocity (VSL) (μm/sec)	Curvilinear velocity (VCL) (μm/sec)	Linearity (VSL/VCL)	Helix diameter (μm)	Helix pitch (μm)	Frequency of rotation (RPS) (rev. per sec)
Mean	54.1	99.1	0.54	3.2	7.4	6.8
Standard Deviation	(± 21.0)	(± 30.3)	(± 0.11)	(± 1.0)	(± 2.0)	(± 4.6)

This table shares the same data as in Fig. 4 *D*, *E*, and *F* of the main text.